New constraints on Xe incorporation mechanisms in olivine from first-principles calculations

Céline Crépisson, Marc Blanchard, Michele Lazzeri, Etienne Balan, Chrystèle Sanloup

New constraints on Xe incorporation mechanisms in olivine from First-principles calculations

Céline Crépisson[a,*], Marc Blanchard[b], Michele Lazzeri[c], Etienne Balan[c], Chrystèle Sanloup[a]

[a]Sorbonne Universités - Institut des Sciences de la Terre de Paris (ISTeP), UPMC Université Paris 06, CNRS, UMR 7193, 4 place Jussieu, 75005, Paris, France

[b]Géosciences Environnement Toulouse, Observatoire Midi-Pyrénées, CNRS UMR 5563, IRD UR 154, Université Paul-Sabatier, 14 avenue Edouard Belin, 31400 Toulouse, France

[c]Sorbonne Universités - Institut de Minéralogie, de Physique des Matériaux, et de Cosmochimie (IMPMC), UPMC Université Paris 06, UMR CNRS 7590, Muséum National d'Histoire Naturelle (MNHN), UMR IRD 206, 4 place Jussieu, 75005 Paris, France

[*]Corresponding author. Address : Céline Crépisson, Institut des Sciences de la Terre de Paris (ISTeP), UPMC Université Paris 06, Case 110, 4 place Jussieu, 75005 Paris, France. Tel.: +33 1 44 27 60 64. Email : celine.crepisson@upmc.fr

Abstract

Storage of Xe at depth in silicate minerals has recently been proposed to explain the low Xe abundance in the Earth's and Mars' atmospheres compared to other noble gases (the so-called 'Missing Xenon' issue). Evidences for incorporation, and thus reactivity of Xe in olivine at high pressure and high temperature are based on variations in cell parameters and the appearance of a new Raman band. To constrain the, so far only hypothetical, Xe incorporation mechanism in olivine, we theoretically investigated models of Xe-bearing olivine using density functional theory. Three types of incorporation mechanisms are tested: Xe for Si and Xe for Mg substitutions, and interstitial Xe. Xe for Si substitution, implying an oxidation of Xe, is found to be the only mechanism consistent with experimental observations, leading to an increase of cell parameter *a* and the appearance of a new Raman band around 720-750 cm^{-1} associated with Xe-O stretching vibrations. Raman spectroscopy makes it possible to identify Xe incorporation site, even at low Xe content, due to high Xe polarizability. An estimation of Xe content in olivine, based on present work and previous *in situ* experimental results, shows that up to 0.4 at % Xe could be stored in olivine at depth.

1.INTRODUCTION

Noble gases, highly volatile and poorly reactive elements, are of particular interest in Earth and planetary sciences to study and date the formation of the atmosphere (Avice and Marty, 2014) or to trace magmatic sources and degassing processes. Xenon, the heaviest of the noble gases, with nine stable isotopes (^{124,126,128,129,130,131,132,134,136}Xe), is at the heart of a long-standing question, the so-called 'Missing Xenon' issue. Elemental Xe, compared to other noble gases, is missing in the atmospheres of the Earth and Mars relative to chondritic abundances (Anders and Owen, 1977). According to Ozima and Podosek (1999), around 90% of Earth's primordial Xe is missing from the atmosphere. In addition, the atmospheres of Earth and Mars present a strong deficit in Xe light isotopes (^{124,126,128}Xe) (Krumennacher, 1962). Some Archean rocks present a Xe isotopic composition falling in between primitive chondritic and present-Earth atmospheric values, with an enrichment of the light non-radiogenic Xe isotopes relative to the present-Earth atmosphere of 2.1 (±0.3) % amu^{-1} for a 3.5 Gy barite (Pujol et al., 2009), and 1 (±0.5) % amu^{-1} for a 3.0 (±0.2) Gy quartz (Pujol et al., 2011). These findings indicate a storage and fractionation of Xe throughout the Archean (Avice and Marty, 2014) which could continue nowadays through subduction processes (Holland and Ballentine, 2006). Recently, a number of studies have supported storage of Xe in silicates at depth. Xe oxides have been synthesized: XeO_2 at ambient pressure and temperature (Brock and Schrobilgen, 2010), and Xe_3O_2 and Xe_2O_5 at respectively 97 GPa and 83 GPa, and at around 2000 K (Dewaele et al., 2016); as well as a Xe-bearing perovskite (Britvin et al., 2015) at ambient pressure. Furthermore, experiments brought evidence of Xe-incorporation in SiO_2 phases (Sanloup et al., 2002, 2005) and olivine (Sanloup et al., 2011) at crustal and upper mantle P-T conditions. If the presence of pure Xe oxides in the Earth is unlikely, storage in silicates as a trace element may be a significant phenomenon in Xe

retention at depth. Furthermore, a granite from the Sudbury impact structure (Kuroda et al., 1977) as well as siliceous sediments (Matsubara et al., 1988; Matsuda and Matsubara, 1989) have been found to be enriched in Xe by 2 to 3 orders of magnitude.

A detailed understanding of incorporation mechanisms of Xe, and reliable values of Xe solubility in minerals are presently needed to quantify the role of Xe incorporation in minerals in the context of the 'Missing Xenon' issue at the Earth's scale. Reliable partition coefficients are also needed to understand the fate of Xe in melting and crystallizing processes (from the magma ocean era to the current day magmatic processes). All available data on Xe-solubility in minerals are based on *ex situ* analyses of Xe-saturated samples, synthesized at high temperatures and, in some cases, at high pressures. Measured Xe solubility in olivine varies from 6.5 ppb down to 0.67 ppt (Broadhurst et al., 1992; Heber et al., 2007; Hiyagon and Ozima, 1986). Similarly, olivine melt partition coefficient varies from 90 to 6.10^{-4} (Broadhurst et al., 1992; Hiyagon and Ozima, 1986; Heber et al., 2007) and the compatibility (or not) of Xe in minerals remains controversial. In samples recovered from high pressure and temperature experiments, Xe is at least partly located in gas bubbles, and inconsistencies in Xe solubility and partition coefficient mainly stem from whether or not bubbles are analyzed, keeping in mind that their sizes range from the nm to the mm scale, and that part or all of these bubbles may form upon quenching to room conditions. Consequently, the evaluation of Xe content should be preferentially based on *in situ* measurements as proposed in the present study.

Recent experiments have focused on the incorporation mechanism of Xe in olivine, one of the most widespread terrestrial minerals. Sanloup et al. (2011) studied Xe-bearing San Carlos olivine up to 7 GPa and 2000 K by *in situ* x-ray diffraction and Raman spectroscopy reporting shifts of lattice parameters in presence of Xe at high pressure and for temperatures above Xe melting point. Cell parameter *a* increases, *c* decreases (although *c* is strongly

101 temperature dependent) while *b* is not affected. This lattice distortion was interpreted as
102 potentially due to Xe incorporation on Si sites, as Si release from olivine was observed. A
103 new Raman mode, in presence of Xe, (disappearing within few minutes after quench) was
104 also observed at 786 cm^{-1} in presence of Xe at 0.9 GPa after heating at 1800 K. This new
105 Raman band is close to the stretching of XeO_4 at 776 cm^{-1} (Gerken and Schrobilgen, 2002),
106 and is in the Si-O stretching region of olivine (Noël et al., 2006). As for other heavy rare
107 gases, Ar was not observed to substitute to Si in olivine up to 7 GPa-2000 K (Sanloup et al.,
108 2011). In the absence of studies devoted to the incorporation of Kr in minerals at depth, we
109 can temporarily conclude that this mechanism is specific to Xe and of major relevance to the
110 'Missing Xe' issue.
111 First-principles calculations represent a powerful complementary approach to identify
112 incorporation sites of trace elements in minerals. Regarding Xe in silicates only two
113 theoretical studies are so far available. Probert (2010) investigated different incorporation
114 mechanisms of Xe in α-quartz, but the lack of related measurements prevents definitive
115 conclusion. Kalinowski et al. (2014) investigated Xe incorporation in fibrous silica, which can
116 be found on Earth in moganite or chalcedoine (Hopkinson et al., 1999). Computed Raman
117 spectra of Xe-bearing fibrous silica possibly reproduce observations for Xe-rich quartz
118 (Sanloup et al., 2002) and XeO_2 (Brock and Schrobilgen, 2011).
119 In the present work, we study the structure, stability and vibrational properties of
120 different incorporation sites of Xe in olivine, by means of first-principles calculations based
121 on density functional theory (DFT). These theoretical results are then compared to the
122 experimental data of Sanloup et al. (2011) to infer potential mechanisms of Xe storage in
123 Earth's interior.
124
125 **2.METHODS**

126

127 Various systems are investigated: two reference compounds (XeO_4 molecule, Xe_3O_2
128 condensed phase); pure forsterite (Mg_2SiO_4, the Mg-rich end member of the olivine series,);
129 Xe-bearing forsterite in which one Xe atom substitutes one Si (or Mg) atom or in which one
130 Xe atom is added at an interstitial position. In all cases, the charge of the simulation cell is
131 neutral. Xe-bearing forsterite is simulated using supercells of various sizes: 2x1x2, 4x1x2,
132 3x1x3, 4x2x4 (with respect to the forsterite unit cell containing 28 atoms) corresponding to a
133 concentration of approximately 0.89, 0.45, 0.40, 0.11 at % Xe (or 5.5, 2.8, 2.5, 0.72 wt %
134 Xe), respectively.
135 All calculations are done within density functional theory (DFT) and the generalized gradient
136 approximation (GGA-PBE) of Perdew et al. (1996), by using the PWscf code of the Quantum
137 ESPRESSO package http://www.quantum-espresso.org/; Gianozzi et al., 2009). Norm-
138 conserving pseudopotentials (Troullier and Martins, 1991) are used. Electronic wave-
139 functions (charge-density) are expanded up to an energy cut-off of 80 (480) Ry. Equilibrium
140 structures are obtained after full relaxation of atomic positions and cell parameters (total
141 energy is converged within 1 mRy/atom and forces to less than 10^{-4} Ry/au). Electronic k-point
142 sampling of Xe_3O_2 and pure forsterite uses 6x16x10 and 2x1x2 shifted grids, while that of the
143 Xe-bearing larger cells uses one shifted k-point. Spin polarized calculations were tested,
144 obtaining zero magnetic moments for all the systems. Vibrational properties (dynamical
145 matrices, dielectric constants, Born effective charges, and Raman tensor) are obtained within
146 the approach of Baroni et al. (2001) and Lazzeri and Mauri (2003). For Raman tensors and
147 effective charges calculations a finer k-point sampling is used (4x2x4 grid for pure forsterite
148 and a 2x2x2 one for Xe-bearing forsterites).
149 For the Xe-bearing forsterites, actual DFT calculations of the dynamical matrices (and, thus,
150 of the interatomic force constants, IFCs) have been done only for the 2x1x2 cell. To simulate

larger cells, we have used a force-matching approach similar to that of Lazzeri and Thibaudeau (2006). One considers a forsterite cell (larger than the 2x1x2 cell) containing one Xe atom: the IFCs among the atoms in the neighborhood of the Xe atom (a sphere centred on the Xe atom with a 6.35 Å radius i.e. containing ~ 80 atoms) are taken from the DFT calculations done on the 2x1x2 cell, the other IFCs (for atoms located further than 6.35 Å from the Xe atom) are taken from pure forsterite bulk calculations.

In the following, calculated Raman spectra are done in a back-scattering geometry and, unless otherwise stated, the spectra are obtained after averaging polarizations and sample orientation. We note that for the kind of systems presently studied, vibrational frequencies are generally underestimated by DFT-GGA calculations. To make the comparison with measurements easier, all theoretical frequencies are multiplied by a factor 1.05 (in order to match the most intense theoretical Raman bands of pure forsterite with the measured ones, Table S1) as in Lazzeri and Mauri (2003).

3.RESULTS

3.1 Reference compounds and pure forsterite

As a test, we calculated the structure of the XeO_4 tetrahedral molecule and Xe_3O_2 condensed phase (Table 1). For XeO_4, Xe-O bond length is 2.0% larger than the experimental value (Gundersen et al., 1970) whereas the one from Probert (2010) is 4.8% larger (Table 1). Xe_3O_2 was simulated at 97 GPa using the orthorhombic *Immm* space group as predicted by Hermann and Schwerdtfeger (2014) and synthesized by Dewaele et al. (2016). Bond lengths are well reproduced (within 0.5%) whereas cell parameters are slightly different (within 1.5%) (Table 1).

Forsterite (Mg_2SiO_4) has an orthorhombic structure with three distinct oxygen sites (O1, O2 and O3), two distinct magnesium sites (Mg1 and Mg2) and one silicon site. Our calculated cell parameters for pure forsterite (a = 4.78 Å, b = 10.25 Å, c = 5.99 Å) are in good agreement with single crystal x-ray diffraction measurements recorded on pure forsterite at ambient conditions, i.e. a = 4.752(3) Å, b = 10.193(8) Å, c = 5.977(5) Å (Hazen et al., 1976). Similar values were obtained by previous studies using also GGA (which tends to increase cell parameters) and similar computational parameters (Balan et al., 2011). Born effective charges (Table S2) and calculated Raman frequencies of pure forsterite (Table S1) are in good agreement with the ones calculated by Noël et al. (2006). Computed polarized Raman spectra are in agreement with McKeown et al. (2011) (Fig. S1). The average Raman spectrum compares well with the experimental spectrum of San Carlos olivine (Sanloup et al., 2011). The presence of Fe in San Carlos olivine ($(Mg_{0.9}Fe_{0.1})_2SiO_4$) does not significantly change the average Raman spectrum compared to pure forsterite (Fig. 5).

3.2 Xe incorporation models

Three main types of Xe incorporation mechanisms are investigated: Xe for Si substitutions (Xe_{Si}), Xe for Mg substitutions (in Mg1 and Mg2 sites) (Xe_{Mg1}, Xe_{Mg2}), and Xe in interstitial site (Xe_i). We relaxed atomic positions at constant volume for these four mechanisms for 0.89 at % Xe. No significant change was observed in the configurations of Xe incorporation sites for more diluted defects (0.45 at % Xe or 0.40 at % Xe, depending on the supercell) or for simultaneous relaxation of atomic positions and cell parameters. The configurations and selected parameters of the four main Xe incorporation sites (Xe_{Si}, Xe_{Mg1}, Xe_{Mg2} and Xe_i) are reported (Figs. 1, 2, 3) following simultaneous relaxation of atomic positions and cell parameters at 0 GPa for 0.89 at % Xe. *.CIF* files for all configurations can

be found in supplementary materials. One third of the trace of the Born effective charge tensor (Z^{eff}) is used to evaluate atomic charges, as discussed by Ghosez et al. (1998).

Xe incorporation sites can be described in terms of the closest surrounding oxygens. Indeed only oxygens are located within the sum of covalent radii that Xe forms with other elements (i.e. ~ 2 Å for oxygen). These oxygens appear to be strongly affected by the presence of Xe in term of variations of Z^{eff} (Figs. 1, 2, 3) compared to pure forsterite (Table S2). For the atoms located beyond the sum of covalent radii no significant variations of Z^{eff} are observed.

3.2.1 Most stable configurations of Xe incorporation sites

For the most stable Xe for Si substitution, Xe is located on the face of the oxygen tetrahedron (Fig. 1). Xe is surrounded by one O1 and two O3 at a distance of ~ 2 Å forming a plane including Xe, with dihedral angles inferior to 2°. Z^{eff} for Xe is slightly more positive than that for Si in pure forsterite (+ 2.85; Table S2). These charges significantly differ from the formal ones (+ 4). This indicates a covalent character of Xe-O bonds involving the closest oxygens (O1 and O3).

Regarding Xe for Mg substitutions, Xe_{Mg2} incorporation site was found more stable than Xe_{Mg1} by 1.05 eV. For both configurations, Xe is located in the former oxygen octahedron. Nevertheless, two oxygen atoms are located close to the sum of covalent radii of Xe and O with Xe-O bond lengths ~ 2 Å whereas others O atoms are located significantly further (Fig. 2). The geometry is nearly linear with angle O3*-Xe-O3* close to 180° for Xe_{Mg2} and O2-Xe-O2 equal to 180° for Xe_{Mg1}. Z^{eff} for Xe in Xe_{Mg1} and Xe_{Mg2} are slightly higher than that for Mg1 (+ 1.95) and Mg2 (+ 2.10) in pure forsterite (Table S2). The small excess of Z^{eff} of Xe in these configurations, compared to charge of Mg in pure forsterite, is

counterbalanced by more negative Z^{eff} for the two closest oxygens (Fig. 2) compared to pure forsterite (Table S2). These results suggest a covalent character of Xe-O bonds involving these oxygens.

For Xe_i, no oxygen atoms are located within the sum of covalent radii of Xe and O (Fig. 3). Z^{eff} for Xe is close to 0 indicating that Xe is nearly neutral in this configuration. Small positive Z^{eff} for Xe, is counterbalanced by slightly more negative Z^{eff} for surrounding oxygens (Fig. 3) compared to pure forsterite (Table S2). However, large Xe-O distances discard the possibility of covalency for Xe-O bond.

3.2.2 Less stable configurations of Xe incorporation sites

For Xe for Si substitution (which was found to best reproduce the experimental observations as further detailed), we investigated possible configurations by slightly moving Xe within the oxygen tetrahedron visible in figure 1. We identified another configuration: $Xe_{Si}(b)$, less stable than Xe_{Si} by 0.54 eV, where Xe is quasi aligned with O1 and O2 (O1-Xe-O2 = 157 °) though Xe remains inside the tetrahedron. For both Xe_{Si} and $Xe_{Si}(b)$ there exist *non symmetric variant* (respectively Xe_{Si}' and $Xe_{Si}(b)$') with Xe slightly shifted toward one of the two O3 of the oxygen tetrahedron so that symmetry of the Xe incorporation sites is broken. These *non symmetric variants* are slightly more stable than the corresponding symmetric variants by 55 meV (for Xe_{Si} and Xe_{Si}') and 54 meV (for $Xe_{Si}(b)$ and $Xe_{Si}(b)$'). We checked that these results are not due to incomplete convergence or artefacts of calculations. A major concern was Van der Waals interactions, which may be crucial for calculations involving noble gases. We therefore repeated our calculations after adding a correction for Van der Waals interactions via a pairwise atomic potential proportional to R^{-6} (with R the distance between the atoms of a pair) as implemented by Barone et al. (2009) for

DFT, based on results from Grimme (2006). We obtained similar geometries for the four configurations and similar relative stabilities as previously found. We only observe a small variation in differences of energies between configurations: from 0.54 eV to 0.68 eV between Xe_{Si} and Xe_{Si}(b) and from 55 meV to 35 meV and from 54 meV to 46 meV, between respectively Xe_{Si} and Xe_{Si}' and Xe_{Si}(b) and Xe_{Si}(b)'.

3.2.3 Comparison with other systems

In our calculation, the most stable Xe for Si substitutions (i.e. Xe_{Si} and Xe_{Si}') present a planar geometry with Xe located on the face of the oxygen tetrahedron, surrounded by one O1 and two O3 (Fig. 1). As emphasized by Kalinowski et al. (2014), a planar structure is common for Xe compounds: in particular under the form of XeO_4 units or chains present in XeO_2 (Brock and Schrobilgen, 2011) Xe_3O_2 and Xe_2O_5 (Dewaele et al., 2016). This planar geometry was also proposed for Xe incorporation in fibrous silica (Kalinowski et al., 2014) and in α-quartz via Xe for Si substitution (Probert, 2011). Other examples of incorporations associated with planar geometries have been reported on boron incorporation in olivine (Ingrin et al., 2014) and carbonate incorporation in fluor-apatite (Yi et al., 2013). In both cases, the carbon and boron atoms share significantly covalent bonds with surrounding oxygens.

Less stable configurations for Xe for Si substitution (i.e. Xe_{Si}(b) and Xe_{Si}(b)'), as well as Xe for Mg substitutions, present nearly linear geometries as in common compounds such as XeF_2 or noble gas hydrides.

For Xe for Si and Xe for Mg substitutions the nearest oxygen atoms have Xe-O bond lengths within the sum of the covalent radii of Xe and O (~ 2 Å) (Figs. 1, 2). Also, the values of Z^{eff} indicate a certain degree of covalency of Xe-O bonds. Xe-O bonds are thus likely to be

279 at least partially covalent for the closest oxygen atoms. This result implies that Xe can react
280 with olivine by oxidation processes.
281
282 3.2.4 Energetics of the Xe-bearing models
283
284 Let us define:
285 $\Delta E(Xe_{Si})=E(Xe_{Si})-E_{Xe}-E_{Fs\text{-}Si}$
286 $\Delta E(Xe_{Mg})=E(Xe_{Mg})-E_{Xe}-E_{Fs\text{-}Mg}$
287 $\Delta E(Xe_i)=E(Xe_i)-E_{Xe}-E_{Fs}$
288
289 where $E(Xe_{Si})$, $E(Xe_{Mg})$, $E(Xe_i)$ are the calculated energies for the cell used to simulate the
290 different type of incorporation mechanisms (Xe_{Si}, Xe_{Mg} and Xe_i). E_{Xe} is the energy of an
291 isolated Xe atom. $E_{Fs\text{-}Si}$ and $E_{Fs\text{-}Mg}$ are the energies of the forsterite cell with one neutral Si or
292 Mg vacancy (the atomic structure was fully relaxed) and E_{Fs} is the energy of a pure forsterite
293 cell. The calculated ΔE values are reported in table 2 and represent the energy of the various
294 incorporations in a forsterite presenting Si and Mg vacancies. Occurrence of Si and Mg
295 vacancies in synthetic forsterite samples is suggested by the observation of related
296 hydroxylated point defects (e.g. Lemaire et al. 2004, Balan et al. 2011, Ingrin et al. 2013,
297 Balan et al. 2017, Blanchard et al. 2017). How the present ΔE values can be compared to
298 measurements is questionable. Indeed, besides the fact that the vacancies in the calculations
299 are neutral, temperature effects are not included. Both effects are expected to be relevant
300 (Verna and Karki, 2009). That said, according to table 2, Xe incorporation in the Si vacancy
301 site (Xe_{Si}) is more stable than Mg-vacancy (Xe_{Mg}) and interstitial (Xe_i) incorporations. A
302 different conclusion would be reached if considering forsterite without vacancies. In this case
303 the relative stability would be dominated by the formation energy of the vacancy itself, which

304 is higher for Si than for Mg (Béjina et al., 2000, Stashans and Flores, 2013), as can be seen in
305 Table 2 by comparing:
306 $\Delta E_v(Si) = E_{Fs\text{-}Si} - E_{Fs} + E_{Si}$
307 $\Delta E_v(Mg) = E_{Fs\text{-}Mg} - E_{Fs} + E_{Mg}$,
308 where E_{Si} and E_{Mg} are the energies of one atom of Si and Mg in the equilibrium diamond and
309 *hcp* bulk, respectively.
310 The relative stability of the three different incorporation mechanisms (Table 2),
311 $\Delta E(Xe_{Si}) < \Delta E(Xe_{Mg}) < \Delta E\ (Xe_i)$, results from an interplay of oxidation state and strain
312 induced on the host structure. Although we cannot unambiguously disentangle these effects
313 and determine which one dominates, we note that there is a correlation between the value of
314 ΔE and the Xe oxidation estimated in Figs. 1-4: the more stable structures having the highest
315 Xe oxidation (as it would be expected if oxidation was the only stabilization mechanism at
316 play). On the other hand, the ΔE ordering can simply reflect the fact that different inclusions
317 correspond to different volume increase of the host forsterite: the more stable structures
318 corresponding to the smaller volume increase (bottom panel of Fig.4), as will be discussed in
319 the next section.
320
321 **3.3 Cell parameters vs. Xe concentration**
322
323 For each configuration, relaxation was done at 0, 2, 5 and 5.7 GPa for 0.89 at % Xe,
324 0.45 at % Xe and 0.40 at % Xe. Cell parameters are only shown at 0 GPa and 5.7 GPa (Fig.
325 4), but the overall trend is similar at 2 GPa and 5 GPa (Table S3). We observe an increase of
326 volume with increasing Xe content (+ 1.6% for Xe for Si substitutions, of + 2.3% for Xe for
327 Mg substitutions, and + 4% for Xe in interstitial site at 0 GPa from 0 at % Xe to 0.89 at %

328 Xe). However, variations of each cell parameters are strongly dependent on the Xe
329 incorporation site (Fig. 4), and this can help to determine the likeliest incorporation site.
330 Variations of cell parameters for Xe_{Si} incorporation site reproduce the experimentally
331 observed increase of cell parameter *a* associated with very small variations of cell parameter *b*
332 (Sanloup et al., 2011) compared to the thermal equation of state of olivine (Liu and Li, 2006).
333 Other incorporation mechanisms do not reproduce this concomitant evolution of *a* and *b*.
334 Experimental variations of cell parameter *c* are strongly temperature dependent (Sanloup et
335 al., 2011), therefore they are not used for comparison with calculations, as they are unlikely to
336 be reproduced quantitatively by our calculations at 0 K. In contrast, the relative variations of *a*
337 and *b*, between the pure and the Xe-bearing systems can be used to assess the concentration of
338 Xe in olivine. For Xe_{Si}, calculated increase of cell parameter *a* from 0 at % Xe to 0.40 at %
339 Xe, is about 0.4% at all investigated pressures. This increase is close to the experimentally
340 observed one (i.e. + 0.2% at 2 GPa, + 0.4% at 5 GPa and + 0.2% at 5.7 GPa). Consequently
341 the Xe content in olivine at high pressure and temperature, studied by Sanloup et al. (2011),
342 can be estimated to be equal or slightly less than 0.40 at % Xe. We note that the Xe content
343 thus determined does not significantly vary with pressure between 2 GPa and 5.7 GPa.
344
345 **3.4 Raman spectra**
346
347 Raman spectra were computed for 0.89 at % Xe (Fig. 5). The two most intense Raman
348 bands of olivine at 822 cm^{-1} and 855 cm^{-1} are clearly visible for Xe_{Si} and Xe_{Mg2} incorporation
349 sites. For Xe_i and Xe_{Mg1} these two olivine bands are mixed with other contributions linked to
350 the presence of Xe. New well-resolved and intense Raman bands appear in the 650-800 cm^{-1}
351 region for Xe_{Si} and, although less intense, for Xe_{Mg1} (Fig. 5). All these new Xe-related Raman
352 bands involve the nearest oxygens around Xe (described and indexed in Figs. 1, 2, 3). For

353 Xe_{Si}, the 720 cm^{-1} band is linked to strong Xe-O1 stretching along the *a* axis (and weak
354 stretching of a SiO_4 tetrahedron close to Xe also along *a* axis), whereas the weak 685 cm^{-1}
355 band is linked to Xe-O2 bending. For Xe_{Mg1} the 739 cm^{-1} band is linked to the two Xe-O2
356 twisting. A new well-resolved intense band is also visible for Xe_{Mg2} at 900 cm^{-1} linked to the
357 two Xe-O3* symmetrical stretching with a wagging component. The bands are visible in
358 parallel polarization along axis or planes corresponding to the maximal direction of the
359 associated vibrational modes (Fig. 5). For Xe_i (which closest oxygen is only located at 2.66
360 Å), no new intense band is observed.

361 For Xe_{Si} and Xe_{Mg}, lots of poorly resolved bands are visible below 650 cm^{-1}, and
362 above 800 cm^{-1}. These weak bands are linked to the high Xe polarizability, which implies that
363 Xe presence will be felt by all atoms of the cell. In order to test this hypothesis, we calculate
364 Raman spectra for lower Xe contents. Results for 0.11 at % Xe are shown in figure 6. Weak
365 non-resolved bands below 650 cm^{-1} and above 800 cm^{-1} visible for 0.89 at % Xe (Fig. 5)
366 disappear with decreasing Xe content. Furthermore, for all Xe incorporation sites, pure
367 forsterite bands are well identified for 0.11 at % Xe not only at 822 cm^{-1} and 855 cm^{-1} but
368 also at 340 cm^{-1}, 611 cm^{-1}, 882 cm^{-1}, 923 cm^{-1}, 964 cm^{-1} (Fig. 6) implying that the presence of
369 Xe is just felt locally as expected for a diluted defect.

370 For 0.11 at % Xe, Raman bands induced by Xe are still visible for Xe_{Si} (at 720 cm^{-1}),
371 Xe_{Mg2} (at 900 cm^{-1}), and Xe_{Mg1} (at 710 cm^{-1}). In contrast, spectra calculated for Xe_i only
372 present minor variations compared to pure forsterite. Presence of Xe in interstitial site can
373 therefore not be evidenced by Raman spectroscopy.

374 We also computed Raman spectra for Xe_{Si}', Xe_{Si}(b) and Xe_{Si}(b)' for 0.89 at % Xe.
375 Spectra show well-defined Xe-related bands at 745 cm^{-1} for Xe_{Si}', 748 cm^{-1} for Xe_{Si} (b) and
376 750 cm^{-1} for Xe_{Si}(b)' (Fig. S2) similar to the Xe-related band at 720 cm^{-1} in Raman spectrum
377 computed for Xe_{Si} (Fig. 5).

The bands observed between 720 cm^{-1} and 750 cm^{-1} for Xe for Si substitutions and at 710 cm^{-1} for Xe_{Mg1} are good candidates to explain the new Raman band observed by Sanloup et al. (2011) (Fig. 6), keeping in mind that only Xe_{Si} reproduces observed variations of cell parameters. Broadness of the experimental Raman band may be caused firstly by the coexistence of Xe_{Si} , Xe_{Si}', Xe_{Si}(b) and Xe_{Si}(b)' at high temperature. It may also be caused by the chemical complexity of San Carlos olivine (see for instance trace and major element analyses of San Carlos olivine in Spandler and O'Neill, 2010). Indeed there exist a variety of Si vacancies, which slightly differs in terms of structural configuration and electronic properties due to Fe and trace elements. Distribution of Xe in these Si vacancies will lead to a range of slightly different vibration modes and consequently to a broad Raman signal as compared to the present ideal model. Eventually, the high temperature of measurement (1800 K) induces broadening of the bands (Kolesov and Geiger, 2004). In cases of band ascribed to chemical defects, this broadening can highly depends on the interaction of the trace element with its crystalline host (e.g. Balan et al., 2017). High temperature may also induce a shift in Raman frequency, as observed for characteristic bands of forsterite (decrease of 15 cm^{-1} from 273 K to 1473 K, Kolesov and Geiger, 2004).

3.4.1 Xe concentration from Raman spectra

Our calculated Raman spectra can be used to approximate the experimental Xe content in olivine. Raman spectrum was computed for 0.45 at % Xe for Xe_{Si} (Fig. 7). The intensity of the Raman spectrum calculated for Xe_{Si} was integrated within the four energy windows shown in figure 7. The intensity was, first, normalized to the integrated intensity in window "3" (corresponding to the characteristic olivine bands) and, then, the contribution from pure forsterite was subtracted. The normalized integrated intensity of Xe-related bands is linearly

403 related to the Xe content (Fig. 8). The corresponding value extracted from the measured
404 Raman spectrum of Xe-rich olivine (Sanloup et al., 2011) is 2.3, which corresponds to ~ 0.2
405 at % Xe in figure 8. This evaluation must be considered as a first approximation and only
406 represents a lower limit due to the significant signal to noise ratio in the experimental
407 spectrum. Comparing Raman spectroscopy and X-ray diffraction, the evaluation of Xe
408 content based on XRD-determined cell-parameters variation (Sec. 3.3) should be more
409 reliable.
410
411 **4.DISCUSSION**
412
413 This work brings new insights on Xe storage at depth, attesting the possibility of Xe
414 incorporation in olivine. We tested here three types of incorporation mechanisms: Xe for Mg
415 and Xe for Si substitutions, and interstitial Xe. Only Xe for Si substitutions can reproduce the
416 observed evolution of the cell parameters induced by Xe at different pressures (Sanloup et al.,
417 2011): the increase of *a* is substantially more important than the increase of *b* (variations of
418 *c*, which are strongly temperature dependent, are unlikely to be reproduced by zero
419 temperature calculations). Furthermore, Xe for Si substitutions induce new Raman bands
420 between 720 cm^{-1} and 750 cm^{-1} comparable with the broad band centred at 786 cm^{-1} observed
421 on Xe-rich San Carlos olivine (Sanloup et al., 2011). Besides these two main results,
422 calculations reported in Table 2 also indicate that Xe for Si substitution might be the most
423 stable from the energetic point of view. The results of table 2 are, however, to be taken only
424 as a temptative estimation of the energetics, since calculations do not include temperature
425 effects and consider vacancies as neutrally charged. Consequently, reactivity of Xe with the
426 olivine is explained by substitution of Xe with silicon inducing Xe oxidation via formation of
427 Xe-O bonds with an important degree of covalency. Presence of Fe and other redox sensitive

trace elements may modulate the reactivity of Xe. Incorporation sites may also slightly change their geometries compared to pure forsterite as studied here.

Raman spectroscopy turns out to be a valuable tool for the study of Xe incorporation in minerals. According to our findings, the high Xe polarizability makes it possible to retrieve a Xe signature for 0.11 at % Xe, and likely below. Moreover, the strong polarization of the Xe-related bands could, in principle, allow to discriminate experimentally among different incorporation mechanisms.

As detailed in the introduction, evaluation of Xe content based on *in situ* measurements is strongly needed. The present calculations can be used to estimate the Xe content in olivine from the *in situ* measurements (Sanloup et al., 2011). This has been done in two independent ways: i) by comparing the calculated and the X-ray diffraction measured values of cell parameters; ii) by comparing the Xe-related Raman-band intensities. According to i) or ii), the Xe concentration is ~ 0.40 at % Xe or ~ 0.20 at % Xe, respectively. We judge 0.40 at % Xe to be more reliable and 0.20 at % Xe should be simply used as a lower boundary. However, the qualitative agreement between the two values is very encouraging, suggesting that future improvements of the present simplified structural model (based on a simple model of iron-free olivine) could provide a theoretical calibration to determine Xe-content from Raman measurements.

Using previously determined Xe solubility value of 0.2 - 0.4 at % for olivine, at 0.9 GPa and 1800 K, and a value of 0.08 mol% Xe for a tholeitic melt at 1.5 GPa and 1773 K (Schmidt and Keppler, 2002), we found a partition coefficient for olivine/tholeitic melt ($^{ol./melt}D_{Xe}$) of 2.5 - 5. A value of $^{ol./melt}D_{Xe}$ close to, or higher than 1, in agreement with Hiyagon and Ozima (1986) and Broadhurst et al. (1992), challenges the supposedly incompatible behaviour of Xe in olivine. However, our value of $^{ol./melt}D_{Xe}$ significantly differs from Heber et al. (2007) ($^{ol./melt}D_{Xe} = 6.10^{-4}$). Heber et al. (2007) evaluated the Xe content of

olivine exclusively on regions free of bubbles and melt inclusions, on the basis that they might have formed upon quenching at ambient conditions, and if so, did not reflect the equilibrium at high pressure and temperature. In contrast Hiyagon and Ozima (1986) and Broadhurst et al. (1992) extracted Xe by heating the whole sample. Our result thus questions the actual quest for free-bubble analysis of recovered samples as a guaranty of reliable estimates of Xe content at high pressure and temperature in corresponding melt or minerals.

Sanloup et al. (2011) observed Xe incorporation in olivine approximately throughout the entire range of lithospheric mantle P/T conditions. Assuming that olivine represents 60% of the mantle volume (Bina, 1998), and that 90% of the Earth's primordial Xe is missing from the atmosphere (Ozima and Podosek, 1999), storing the entire amount of the 'Missing Xe' in the olivine of the upper mantle requires a Xe content in olivine of 0.012 ppb. This estimate is much lower than the solubility value of 0.4 at % (i.e. 2.5 wt % Xe) found here, hence the entire amount of the 'Missing Xe' could be stored in the upper mantle.

Although more data are needed on the dependence of Xe solubility in olivine on olivine chemical composition (e.g. Fe and other trivalent cations), pressures and temperatures, but also in other minerals, these preliminary results prove that storage of Xe at depth can no longer be discarded in the 'Missing Xenon' issue.

To our knowledge, there is currently no data available on the potential isotopic fractionation of Xe during incorporation in minerals. However, it could be a key to explain particular terrestrial Xe isotopic compositions, such as the observed ^{136}Xe enrichment in mantle xenoliths of Mt Quincan (North Queensland, Australia), Victoria (Southeastern Australia) and Reunion Island, which cannot be explained by mass dependent fractionation (Czuppon et al., 2009).

ACKNOWLEDGEMENTS

We are grateful to Yves Noël for helpful discussions. Calculations were performed using the IBM iDataPlex cluster of the UPMC. This work was supported by the European Community's Seventh Framework Programme (FP7/2007-2013) under grant agreements no. 312284 and 259649 (European Research Council starting grant to C. Sanloup).

REFERENCES

Anders E. and Owen T. (1977) Mars and Earth: Origin and Abundance of volatiles. *Science* **198**, 453-465.

Avice G. and Marty B. (2014) The iodine–plutonium–xenon age of the Moon–Earth system revisited. *Phil. Trans. Soc.* **A 372**, 20130260-20130276.

Balan E., Ingrin J., Delattre S., Kovács I., Blanchard M. (2011) Theoretical infrared spectrum of OH-defects in forsterite. *Eur. J. Mineral.* **23**, 285–292.

Balan E., Blanchard M., Lazzeri M., Ingrin J. (2017) Theoretical Raman spectrum and anharmonicity of tetrahedral OH defects in hydrous forsterite. *Eur. J. Mineral*. **29**, 201-212.

Barone V., Casarin M., Forrer D., Pavone M., Sambi M. and Vittadini A. (2009) Role and Effective Treatment of Dispersive Forces in Materials: Polyethylene and Graphite Crystals as Test Cases. *J. Comput. Chem.* **30**, 934-939.

Baroni S., de Gironcoli S., Dal Corso A. and Giannozzi P. (2001) Phonons and related crystal

503 properties from density-functional perturbation theory, *Rev. Mod. Phys.* **73**, 515-562.
504
505 Béjina F., Blanchard M., Wright K. and Price G.D. (2009) A computer simulation of the
506 effect of pressure on Mg diffusion in forsterite. *Phys. Earth Planet. Int.* **172**, 13-19.
507
508 Bina C. R. (1998) Olivine emerges from isolation, *Nature* **392**, 650-653.
509
510 Blanchard M., Ingrin J., Balan E., Kovacs I., Withers A.C. (2017) Effect of iron and trivalent
511 cations on OH-defects in olivine. *Am. Mineral.* **102**, 302-311.
512
513 Britvin S. N., Kashtanov S. A., Krzhizhanovskaya M. G., Gurinov A. A., Glumov O. V.,
514 Strekopytov S., Kretser Y. L., Zaitsev A. N., Chukanov N. V. and Krivovichev S. V. (2015)
515 Perovskites with the Framework-Forming Xenon. *Angew. Chem. Int. Ed.* **48**, 14340-14344.
516
517 Broadhurst C. L., Drake M. J., Hagee B. E. and Bernatowicz T. J. (1992) Solubility and
518 partitioning of Ne, Ar, and Xe in minerals and synthetic basaltic melts., *Geochim.*
519 *Cosmochim. Acta* **56**, 709-723.
520
521 Brock D. S. and Schrobilgen G. J. (2011) Synthesis of the Missing Oxide of Xenon, XeO_2,
522 and its implications for Earth's Missing Xenon. *J. Am. Chem. Soc.* **133**, 6265–6269.
523
524 Crépisson C., Blanchard M., Bureau H., Sanloup C., Withers A. C., Khodja H., Surblé S.,
525 Raepsaet C., Béneut K., Leroy C., Giura P. and Balan E. (2014) Clumped fluoride-hydroxyl
526 defects in forsterite: Implications for the uppe-mantle. *Earth and Planet. Sci. Lett* **390**, 287–
527 295.

528

529 Czuppon G., Matsumoto T., Handler M. R. and Matsuda J.-I. (2009) Noble gases in spinel
530 peridotite xenoliths from Mt Quincan, North Queensland, Australia: undisturbed morb-type
531 noble gases in the subcontinental lithospheric mantle. *Chem. Geol.* **266**, 19–28.

532

533 Dewaele A., Worth N., Pickard C. J., Needs R.J., Pascarelli S., Mathon O., Mezouar M. and
534 Irifune T. (2016) Synthesis and stability of xenon oxides Xe_2O_5 and Xe_3O_2 under pressure.
535 *Nature Chemistry* **8**, 784.

536

537 Gerken M. and Schrobilgen G. J. (2002) Solution Multi-NMR and Raman Spectroscopic
538 Studies of Thermodynamically Unstable XeO4. The First ^{131}Xe NMR Study of a Chemically
539 Bound Xenon Species. *Inorg. Chem.,* **41(2),** 198–204.

540

541 Ghosez Ph., Michenaud J.-P. and Gonze X. (1998) Dynamical atomic charges: the case of
542 ABO_3 compounds. *Phys. Rev. B* **58**, 6224-6240.

543

544 Giannozzi P., Baroni S., Bonini N., Calandra M., Car R., Cavazzoni C., Ceresoli D., Chiarotti
545 G.L., Cococcioni M., Dabo I., Dal Corso A., de Gironcoli S., Fabris S., Fratesi G., Gebauer
546 R., Gerstmann U., Gougoussis C., Kokalj A., Lazzeri M., Martin-Samos L. (2009) quantum
547 ESPRESSO: a modular and open-source software project for quantum simulations of
548 materials. *J. Phys.: Condens. Matter* **21**, 395502-395521.

549

550 Grimme S. (2006) Semiempirical GGA-Type Density Functional Constructed with a Long-
551 Range Dispersion Correction. *J. Comput. Chem.* **27**, 1787-1799.

552

553 Gundersen G., Hedberg K. and Huston J. L. (1970) Molecular Structure of Xenon Tetroxide,
554 XeO_4. *J. Chem. Phys.* **52**, 812-813.
555
556 Hazen R. M. (1976) Effects of temperature and pressure on the crystal structure of forsterite.
557 *Am. Mineral.* **61**, 1280-1293.
558
559 Heber V. S., Brooker R. A., Kelley S. P. and Wood B. J. (2007) Crystal-melt partitioning of
560 noble gases (helium, neon, argon, krypton, and xenon) for olivine and clinopyroxene.
561 *Geochim. Cosmochim. Acta* **71**, 1041-1061.
562
563 Hermann A. and Schwerdtfeger P. (2014) Xenon Suboxides Stable under Pressure. *J. Phys.*
564 *Chem. Lett.* **5**, 4336-4342.
565
566 Hiyagon H. and Ozima M. (1986) Partition of noble gases between olivine and basalt melt.
567 *Geochim. Cosmochim. Acta* **50**, 2045-2057.
568
569 Holland G. and Ballentine C. J. (2006) Seawater subduction controls the heavy noble gas
570 composition of the mantle. *Nature* **441**, 186-191.
571
572 Hopkinson L., Roberts S., Herrington R. and Wilkinson J. (1999) The nature of crystalline
573 silica from the TAG submarine hydrothermal mound, 26°N Mid Atlantic Ridge. *Contrib*
574 *Mineral Petrol* **137**, 342-350.
575

576 Ingrin J., Liu J., Depecker C., Kohn S.C., Balan E., Grant K.J. (2013) Low-temperature
577 evolution of OH bands in synthetic forsterite, implication for the nature of H defects at high
578 pressure. *Phys. Chem. Minerals* **40**, 499-510.
579
580 Ingrin J., Kovacs I., Deloule E., Balan E., Blanchard M., Kohn S.C. and Hermann J. (2014)
581 Identification of hydrogen defects linked to boron substitution in synthetic forsterite and
582 natural olivine. *Am. Mineral.* **99**, 2138-2141.
583
584 Kalinowski J., Räsänen M. and Gerber R. B. (2014) Chemically-bound Xenon in Fibrous
585 Silica. *Phys. Chem. Chem. Phys.* **16**, 11658-11663.
586
587 Kolesov A. and Geiger C. A. (2004) A Raman spectroscopic study of Fe–Mg olivines. *Phys.*
588 *Chem. Minerals* **31**, 142-154.
589
590 Krumennacher D., Merrihue C. M., Pepin R. O. and Reynolds J. H. (1962) Meteoritic krypton
591 and barium versus the general isotopic anomalies in meteoritic xenon. *Geochim. Cosmochim.*
592 *Acta* **28**, 231-249.
593
594 Kuroda P. K., Sherrill R. D. and Jackson K. C. (1977) Abundances and isotopic compositions
595 of rare gases in granites. *Geochem. J.* **11**, 75-90.
596
597 Lazzeri M. and Mauri F. (2003) First-Principles Calculation of Vibrational Raman Spectra in
598 Large Systems: Signature of Small Rings in Crystalline SiO_2. *Phys. Rev. Lett.* **90**, 036401-
599 036405.
600

601 Lazzeri M. and Thibaudeau P. (2006) *Ab initio* Raman spectrum of the normal and disordered
602 $MgAl_2O_4$ spinel. *Phys. Rev. B.* **74**, 140301-140305.
603
604 Lemaire C., Kohn S.C., Brooker R.A. (2004) The effect of silica activity on the incorporation
605 mechanism of water in synthetic forsterite: a polarised infrared spectroscopic study. *Contrib.*
606 *Mineral. Petrol*. **147**, 48-57.
607
608 Liu W. and Li B. (2006) Thermal equation of state of $(Mg_{0.9}Fe_{0.1})_2SiO_4$ olivine. *Phys. Earth*
609 *Planet. Int.* **157**, 188-195.
610
611 Matsubara K., Matsuda J., Nagao K., Kita I. and Taguchi S. (1988) Xe in amorphous silica: a
612 new thermometer in geothermal systems. *Geophys. Res. Lett.* **15(7)**, 657-660.
613
614 Matsuda J. and Matsubara K. (1989) Noble gases in silica and their implication for the
615 terrestrial "Missing" Xe. *Geophys. Res. Lett.* **16 (1)**, 81-84.
616
617 McKeown D., Bell M. I. and Caracas R. (2010) Theoretical determination of the Raman
618 spectra of single-crystal forsterite (Mg_2SiO_4). *Am. Mineral.* **95**, 980–986.
619
620 Noël Y., Catti M., d'Arco P. and Dovesi R. (2006) The vibrational frequencies of forsterite
621 Mg_2SiO_4: an all-electron *ab initio* study with the CRYSTAL code. *Phys. Chem. Minerals* **33**,
622 383-393.
623
624 Ozima M. and Podosek F. A. (1999) Formation age of Earth from 129I/127I and 244Pu/238U
625 systematics and the missing Xe. *J. Geophys. Res.* **104 (B11),** 25493-25499.

626

627 Perdew J.P., Burke K. and Ernzerhof M. (1996) Generalized gradient approximation made
628 simple. *Phys. Rev. Lett.* **77**, 3865-3868.

629

630 Probert M.I.J. (2010) An *ab initio* study of xenon retention in α-quartz. *J. Phys.: Condens.*
631 *Matter* **22**, 025501-025511.

632

633 Pujol M., Marty B. and Burgess R. (2011) Chondritic-like xenon trapped in Archean rocks: A
634 possible signature of the ancient atmosphere. *Earth Planet. Sci. Lett.* **308**, 298–306.

635

636 Pujol, M., Marty, B. and Burgess R. (2013) Reply to comment on "Chondritic-like xenon
637 trapped in Archean rocks: A possible signature of the ancient atmosphere" by Pujol, M.,
638 Marty, B., Burgess, R. by Pepin, R.O., Earth and Planetary Science Letters 308 (2011) 298-
639 306 . *Earth Planet. Sci. Lett.* **371**, 296-298.

640

641 Sanloup C., Hemley R. J. and Mao H-K. (2002) Evidence for xenon silicates at high pressure
642 and temperature. *Geophys. Res. Lett.* **29**, 1883-1887.

643

644 Sanloup C., Schmidt B. C., Chamorro Perez E. M., Jambon A., Gregoryanz E. and Mezouar
645 M. (2005) Retention of Xenon in Quartz and Earth's Missing Xenon. *Science* **310**, 1174-
646 1177.

647

648 Sanloup C., Schmidt B. C., Gudfinnsson G., Dewaele A. and Mezouar M. (2011) Xenon and
649 Argon: a contrasting behaviour in olivine at depth. *Geochim. Cosmochim. Acta* **75**, 6271–
650 6284.

651

652 Schmidt B.C. and Keppler H. (2002) Experimental evidence for high noble gas solubilities in
653 silicate melts under mantle pressures, *Earth Planet. Sci. Lett.* **195**, 277-290.

654

655 Spandler C. and O'Neill H. St.C. (2010) Diffusion and partition coefficients of minor and
656 trace elements in San Carlos olivine at 1,300°C with some geochemical implications. *Contrib.*
657 *Mineral. Petrol.* **159**, 791-818.

658

659 Stashans A. and Flores Y. (2013) Modelling of neutral vacancies in forsterite mineral *Int. J.*
660 *Mod. Phys. B.* **27**, 1350141.

661

662 Troullier N. and Martins J. L. (1991) Efficient pseudopotentials for plane-wave calculations.
663 *Phys. Rev. B* **43**, 1993-2006.

664

665 Verma A. K. and Karki B. B. (2009) Ab initio investigations of native protonic point defects
666 in Mg_2SiO_4 polymorphs under high pressure. *Earth Planet. Sci. Lett.* **285**, 140-149.

667

668 Yi H., Balan E., Gervais C., Segalen L., Fayon F., Riche D., Person A., Morin G., Guillaumet
669 M., Blanchard M., Lazzeri M. and Babonneau F. (2013) A carbonate-fluoride defect model
670 for carbonate-rich fluorapatite. *Am. Mineral*. **98**, 1066-1069.

671

672

673

674

675

Table 1: Bond lengths and cell parameters of Xe reference compounds: XeO_4 molecule and Xe_3O_2 at 97 GPa.

XeO_4	**This study**	**Calc.[a]**	**Exp.[b]**
Xe - O (Å)	1.77	1.82	1.736
Xe_3O_2	**This study**	**Calc.[c]**	**Exp.[c]**
a (Å)	8.377	8.388	8.457
b (Å)	3.206	3.195	3.166
c (Å)	4.881	4.881	4.904
Xe^{4+}- O (Å)	2.01	2.01	1.99
Xe^0-Xe^0 (Å)	3.05	3.05	3.06
Xe^{4+}-Xe^0 (Å)	2.95-3.00	2.95-3.00	2.96-3.01
Xe^{4+}- Xe^{4+} (Å)	3.21	3.19	3.17

[a] Probert, 2010, [b] Gundersen et al. (1970), and [c] Dewaele et al. (2016).

Table 2: Formation energies for the different Xe incorporation mechanisms. ΔE and ΔE_v are defined in the text.

	ΔE (eV)		ΔEv (eV)
Xe_{Si}	-0.12	Si	15.2
Xe_{Mg1}	2.75	Mg_1	8.9
Xe_{Mg2}	1.48	Mg_2	10.0
Xe_i	8.21		

721 **Figure captions**

722

723 Figure 1: Calculated structure of the Xe_{Si} incorporation site in forsterite. Note the localization
724 of the Xe on the face of the oxygen tetrahedron. Relevant O-Xe-O angles, Xe-O bond length,
725 and one third of the trace of the Born effective charge tensor (Z^{eff}) are indicated. *a*,*b*, and *c*
726 forsterite lattice parameters are along x, y, and z axes, respectively.

727

728 Figure 2: Calculated structure of the Xe_{Mg1} and Xe_{Mg2} incorporation sites (see also Fig.1
729 caption). O3 and O3* atoms are equivalent in pure forsterite.

730

731 Figure 3: Calculated structure of the Xe_i incorporation site (see also Fig.1 caption).
732 O3a/O3b/O3c/O3d atoms (as O2/O2* and O1/O1*) are equivalent in pure forsterite. For
733 clarity, only details for O within 3.05 Å around Xe are given.

734

735 Figure 4: Calculated evolution of cell parameters *a*, *b*, *c* and volume as a function of Xe
736 content at 0 GPa (black symbols) and 5.7 GPa (orange symbols). Dotted lines are guides for
737 the eyes.

738

739 Figure 5: Calculated Raman spectra of the different stable configurations of Xe incorportation
740 in forsterite (0.89 at % Xe) and pure forsterite vs. measurements (exp.) from Sanloup et al.
741 (2011). The spectrum on Xe-rich olivine was recorded at 0.9 GPa after quenching T from
742 1800 K. The spectrum on Xe-free olivine was recorded at 0.9 GPa and 300 K before heating
743 (i.e. before reaction of Xe with olivine). The labels associated with some calculated Xe-
744 related bands indicate strong polarization: the bands are visible only in parallel polarization
745 along specific axes (corresponding to the *a*,*b*,*c* lattice parameters).

Figure 6: Calculated Raman spectra of the different stable configurations of Xe incorporation in forsterite (0.11 at % Xe) and pure forsterite vs. measurements (exp.) from Sanloup et al. (2011).

Figure 7: Calculated Raman spectra for Xe_{Si} for various Xe content. Measurements (exp.) from Sanloup et al. (2011). The four energy windows (1, 2, 3 and 4) used to integrate the intensity of Raman bands (see text) are shown.

Figure 8: Normalized integrated intensity of Xe-related Raman bands for Xe_{Si} incorporation site as a function of Xe content from the present calculations. The dotted line is a linear fit. The horizontal dashed line indicates value for experimental Raman spectrum of Xe-rich olivine from Sanloup et al. (2011).

Figure 1

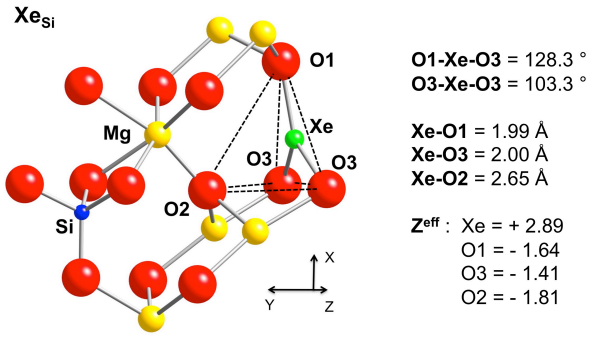
Xe$_{Si}$
O1
Mg
Xe
O3
O3
Si
O2
X
Y
Z
O1-Xe-O3 = 128.3 °
O3-Xe-O3 = 103.3 °
Xe-O1 = 1.99 Å
Xe-O3 = 2.00 Å
Xe-O2 = 2.65 Å
Z^{eff} : Xe = + 2.89
O1 = - 1.64
O3 = - 1.41
O2 = - 1.81

Figure 2

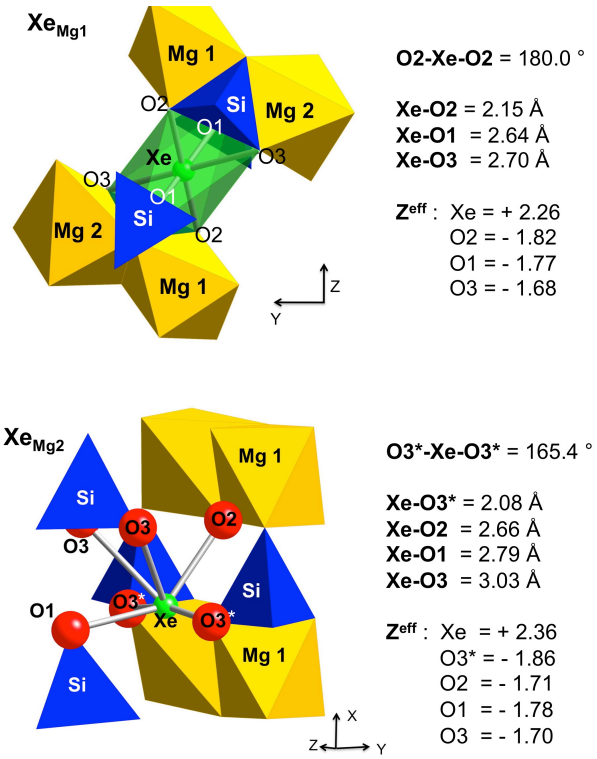
Xe$_{Mg1}$
Mg 1
Si
Mg 2
O2
O1
Xe
O3
O3
O1
Si
Mg 2
O2
Mg 1
Z
Y
O2-Xe-O2 = 180.0 °
Xe-O2 = 2.15 Å
Xe-O1 = 2.64 Å
Xe-O3 = 2.70 Å
Z^{eff} : Xe = + 2.26
O2 = - 1.82
O1 = - 1.77
O3 = - 1.68
Xe$_{Mg2}$
Mg 1
Si
O3
O2
O3
Si
O1
O3*
Xe
O3*
Mg 1
Si
X
Z
Y
O3*-Xe-O3* = 165.4 °
Xe-O3* = 2.08 Å
Xe-O2 = 2.66 Å
Xe-O1 = 2.79 Å
Xe-O3 = 3.03 Å
Z^{eff} : Xe = + 2.36
O3* = - 1.86
O2 = - 1.71
O1 = - 1.78
O3 = - 1.70

Figure 3

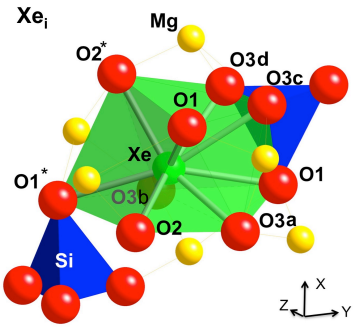

Xe-O3a = 2.66 Å
Xe-O2* = 2.66 Å
Xe-O3b = 2.79 Å
Xe-O1* = 2.84 Å
Xe-O3c = 2.90 Å

Z^{eff} : Xe = + 0.30
O3a = - 1.82
O2* = - 1.78
O3b = - 1.76
O1* = - 1.83
O3c = - 1.79

Figure 4

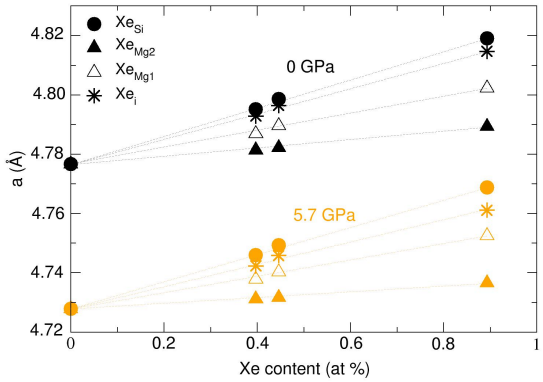
Xe_Si
Xe_Mg2
Xe_Mg1
Xe_i
0 GPa
5.7 GPa
a (Å)
Xe content (at %)

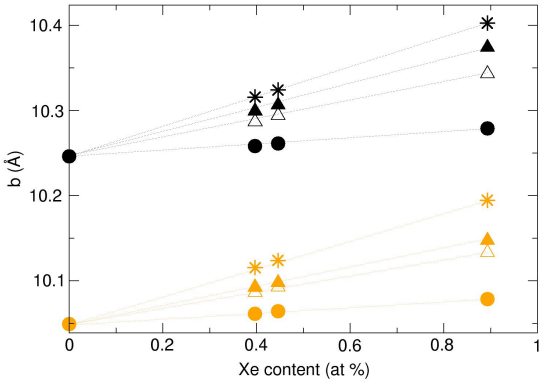
b (Å)
Xe content (at %)

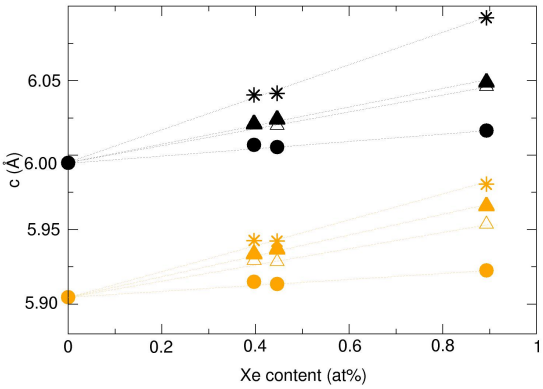
c (Å)
Xe content (at%)

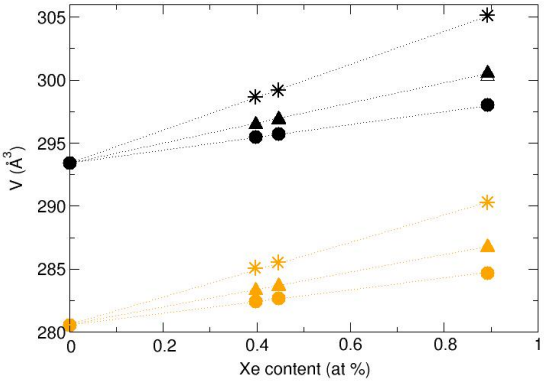
V (Å^3)
Xe content (at %)

Figure 5

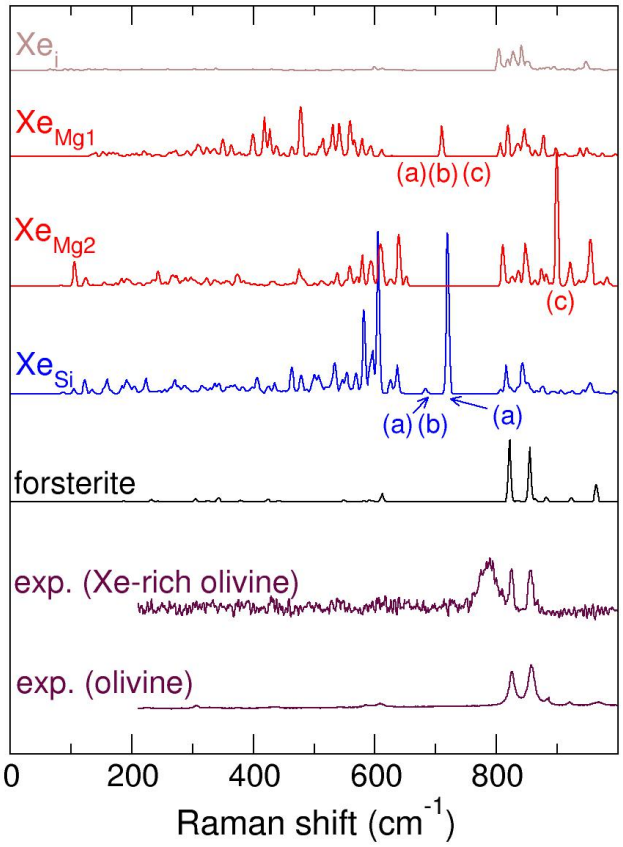
Xe$_i$
Xe$_{Mg1}$
(a)(b)(c)
Xe$_{Mg2}$
(c)
Xe$_{Si}$
(a)(b)
(a)
forsterite
exp. (Xe-rich olivine)
exp. (olivine)
0
200
400
600
800
Raman shift (cm^{-1})

Figure 6

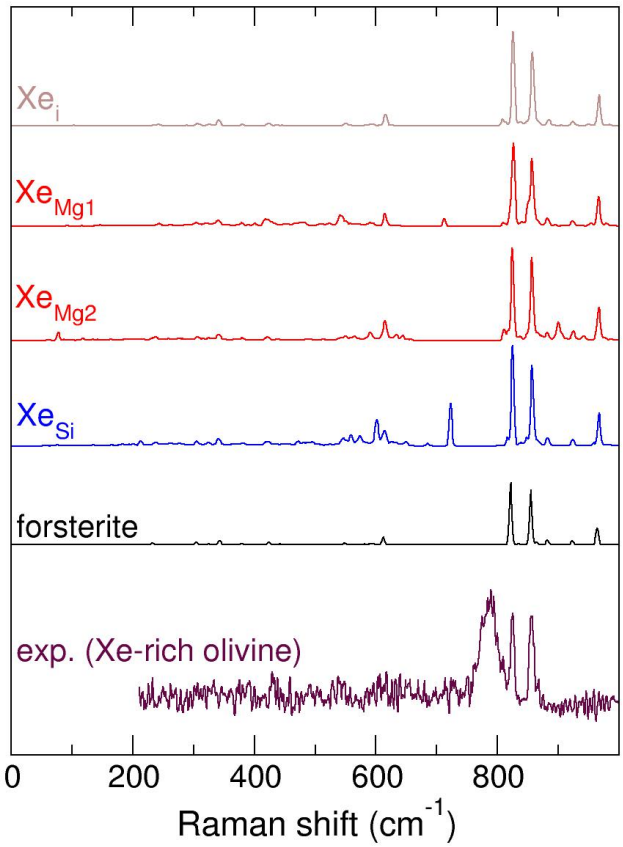
Xe$_i$
Xe$_{Mg1}$
Xe$_{Mg2}$
Xe$_{Si}$
forsterite
exp. (Xe-rich olivine)
0
200
400
600
800
Raman shift (cm^{-1})

Figure 7

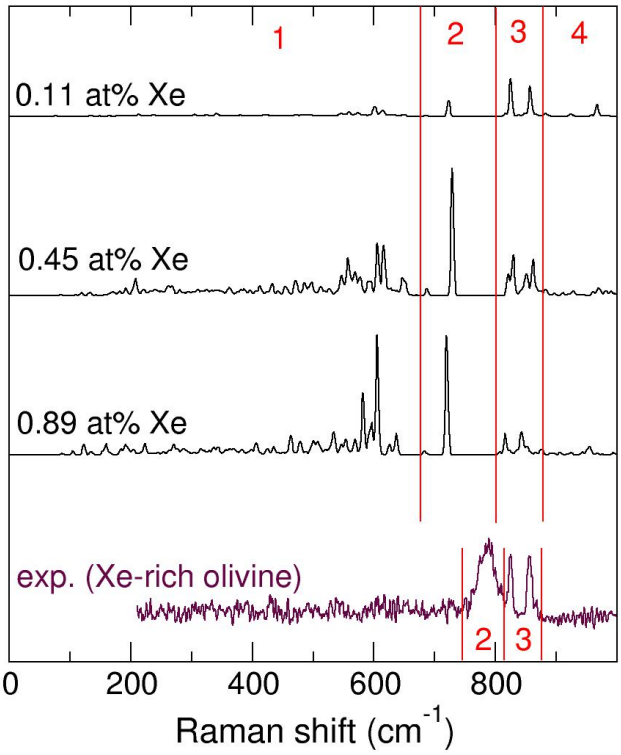
1
2
3
4
0.11 at% Xe
0.45 at% Xe
0.89 at% Xe
exp. (Xe-rich olivine)
2
3
0
200
400
600
800
Raman shift (cm-1)

886 **Figure 8**

887

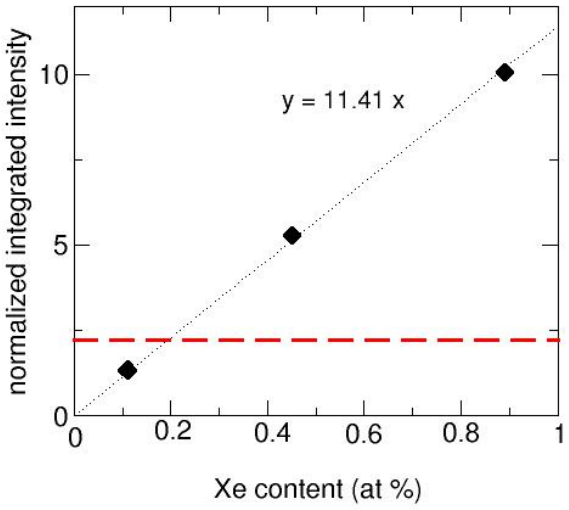

888